Structural Stability from Crystallographic Shear in TiO_2–Nb_2O_5 Phases: Cation-ordering and Lithiation Behavior of $TiNb_{24}O_{62}$

Kent J. Griffith[1], Anatoliy Senyshyn[2], Clare P. Grey[1*]

[1] Department of Chemistry, University of Cambridge, Lensfield Road, Cambridge, CB2 1EW, United Kingdom

[2] Heinz Maier-Leibnitz Zentrum, Technische Universität München, Lichtenbergstrasse 1, 85748 Garching b. München, Germany

[*]cpg27@cam.ac.uk

ABSTRACT: The host structure and reversible lithium insertion and extraction into an intercalation compound, $TiNb_{24}O_{62}$, are described. Neutron diffraction, applied for the first time to $TiNb_{24}O_{62}$, allowed an accurate refinement of the complex block superstructure, particularly with respect to the oxygen sublattice. Analysis of the transition metal sites revealed significant cation-ordering in the mixed metal oxide. Electrochemical analysis demonstrated highly reversible lithium intercalation with *ca.* 190 $mA \cdot h \cdot g^{-1}$ after 100 cycles (C/10 rate, three months). The effect of potential window on capacity, polarization, and reversibility was carefully examined; a minimum voltage limit of 1.1–1.2 V is critical for efficient and reversible cycling. The galvanostatic intermittent titration technique revealed three solid-solution regions, with different Li diffusivities, in addition to the two-phase plateau that was clearly observed in the V vs. Q discharge/charge profile. Lithium-ion diffusion decreases by over three orders-of-magnitude from the dilute lithium limit early in the discharge to the lithium-stuffed phase $Li_{37.5(1.0)}TiNb_{24}O_{62}$. Nevertheless, prior to lithium-stuffing, $TiNb_{24}O_{62}$ possesses intrinsically rapid lithium-ion kinetics as demonstrated by high-rate performance in thick films of *ca.* 10 μm particles when interfaced with a carbon-coated aluminum foil substrate. The $TiO_2 \cdot Nb_2O_5$ phase diagram is examined and electrochemical results are compared to related superstructures of crystallographically sheared blocks of octahedra in the $TiO_2 \cdot Nb_2O_5$ homologous series including the H-Nb_2O_5 end-member.

1. INTRODUCTION

High-voltage anodes for lithium-ion batteries, loosely defined as materials with a lower voltage limit above 1.0 V vs. Li^+/Li, offer promising advantages in terms of safety and cycle life. Carbonate electrolytes are not stable below *ca.* 1.0 V and traditional lithium battery anodes rely on the formation of a stable solid–electrolyte interphase (SEI) layer. As a result, high surface area nanoparticles as well as alloying electrodes that undergo large volume changes on cycling both consume substantial electrolyte and lithium, which is associated with poor capacity retention. In addition, during low voltage discharge, inhomogeneity in the anode electrode may lead to local

regions experiencing a sufficiently low potential to promote lithium dendrite formation. Cell degradation and dangerous internal short-circuits from dendrite formation can be avoided with a high-voltage anode, at the expense of energy density.

Several high-voltage intercalation anode candidates have been investigated. The most studied is $Li_4Ti_5O_{12}$ (LTO) which, due to the advantages addressed above, has matured to the commercial level. While LTO performs well, it has several known issues. Relatively low gravimetric and volumetric capacity leave room for improvement but the most pressing issue is the significant gas generation and swelling observed with LTO electrodes. The gases, mostly H_2, CO_2, and CO, are formed via reactions between standard alkyl carbonate solvents and the LTO interface[1]. These issues motivate the search for next generation safe anode materials. Cava *et al.* first reported the lithiation, primarily chemical lithiation with *n*-butyllithium, of a wide range Nb-based high-voltage anodes in a seminal work in the early 1980s[2]. However, it was not until relatively recently that electrochemical studies on Nb_2O_5[3–5] and some mixed metal oxides such as $TiNb_2O_7$[2,6–8] and $Ti_2Nb_{10}O_{29}$[9,10] have resumed with vigor. To our knowledge, the electrochemical lithiation of $TiNb_{24}O_{62}$ has not been thoroughly investigated, though 0.6 lithium per transition metal were found to intercalate chemically[2], which corresponds to a capacity of 120 $mA{\cdot}h{\cdot}g^{-1}$ compared to the theoretical capacity of 204.9 $mA{\cdot}h{\cdot}g^{-1}$ for a one electron reduction.

Structurally, $TiNb_{24}O_{62}$ falls into a large family of materials known as Wadsley–Roth phases derived from the ReO_3 structure. Several oxides with the composition MO_3 (e.g. β-MoO_3, α-, β-, γ-WO_3, ReO_3) assemble into a structure of corned-shared MO_6 octahedra. The octahedra are

distorted to varying degrees based on the strength of the second-order Jahn–Teller (SOJT) effect, which increases with formal charge and decreases with cation size for the d^0 transition metals.[11] Anion deficient oxides of MO_{3-x} (e.g. V_6O_{13}, $NbO_{2.5(-x)}$, MoO_{3-x}, WO_{3-x}) with metal valence less than M(VI) cannot form the perfect ReO_3-type arrangement and thus adopt a defect structure. One common motif is to form planes of edge-sharing octahedra creating so-called crystallographic shear (*cs*) planes, two such intersecting planes define the edges of a length $m \times n$ block of octahedra.[12] The resulting structure, known as a Wadsley–Roth or *cs* phase[2], can consist of blocks connected in infinite ribbons ($p = \infty$), split into pairs ($p = 2$), or isolated ($p = 1$), usually by tetrahedra. The nomenclature $(m \times n)_p$ then fully describes the assembly of structural units though the description may be further complicated by the presence of multiple block sizes and intergrowths even within ordered "ideal" phases. From these principles, the composition of a block is dictated by the crystal structure and the metal oxide formula can be calculated from a summation over all combinations of block size and connectivity:

$$\sum M_{mnp+1}O_{3mnp-(m+n)p+4}$$

where interconnected ribbons may be represented by:

$$\lim_{p\to\infty} M_{mnp+1}O_{3mnp-(m+n)p+4} = M_{mn}O_{3mn-(m+n)}$$

$TiNb_{24}O_{62}$ (i.e. $TiO_2{\cdot}12Nb_2O_5$)[13] is the Nb-rich end member of a series of structurally and compositionally related Ti–Nb–O ternary shear phases including $TiNb_2O_7$ ($TiO_2{\cdot}Nb_2O_5$) and $Ti_2Nb_{10}O_{29}$ ($2TiO_2{\cdot}5Nb_2O_5$). $Ti_2Nb_{10}O_{29}$ has two known polymorphs: monoclinic-$Ti_2Nb_{10}O_{29}$ (*m*-$Ti_2Nb_{10}O_{29}$) crystallizes from an amorphous solid at 810–835 °C and transforms to the orthorhombic polymorph (*o*-$Ti_2Nb_{10}O_{29}$) at 1200–1300 °C.[14] Evidence from electron diffraction suggests the presence of domains of other TiO_2–Nb_2O_5 intergrowth phases, e.g. intergrowths between H-Nb_2O_5 and $TiNb_{24}O_{62}$: $TiNb_{38}O_{97}$, $TiNb_{52}O_{132}$,[15–17] but they have not been isolated as

phase-pure samples. In this family of compounds, the ribbon-breaking MO_4 tetrahedra in $TiNb_{24}O_{62}$ $(3 \times 4)_2$ are not found in $TiNb_2O_7$ $(3 \times 3)_\infty$ or either polymorph of $Ti_2Nb_{10}O_{29}$ $(3 \times 4)_\infty$ though they are present in the aforementioned intergrowth structures.

Cheetham and Von Dreele[18,19] first used neutrons to study the structure and cation distribution in the Wadsley–Roth phases $TiNb_2O_7$ and *o*-$Ti_2Nb_{10}O_{29}$ at 4.2 K.[18,19] The large scattering cross section of oxygen in a neutron beam versus an X-ray source, relative to titanium and niobium, enabled a much higher quality determination of the oxygen sublattice. Furthermore, the nuclear coherent scattering length of titanium (–3.438 fm) and niobium (7.054 fm) differ in sign and magnitude and thus the metal site occupancies can be readily determined. The titanium occupancy was found to vary from 14.0–64.5% in $TiNb_2O_7$ and from 4.5–40.0% in *o*-$Ti_2Nb_{10}O_{29}$.[19] Neutron powder diffraction served as a complementary probe to earlier X-ray studies and, together, they provided some insight into the SOJT-distorted polyhedra and cation-ordering in these complex titania–niobia *cs* phases.

In this work, we begin with an accurate refinement of the lattice and atomic coordinates of the $TiNb_{24}O_{62}$ structure via high-resolution neutron powder diffraction (NPD). The refined structure includes a determination of cation-ordering related to the block structure and significantly improved oxygen positions, yielding bond valence sums (BVS) close to the predicted values of four and five for Ti^{4+} and Nb^{5+}, respectively. After establishing the host structure, we report a detailed electrochemical investigation of $TiNb_{24}O_{62}$ as a lithium-ion battery intercalation electrode and evaluate the stability window over long-term cycling and the effects of kinetics and thermodynamics as a function of lithiation. High intercalation capacity, exceptionally stable

cycle life, and bulk high-rate performance are demonstrated. The structure and properties of $TiNb_{24}O_{62}$ are discussed in the context of related crystallographic shear structures and mixed TiO_2–Nb_2O_5 structures, which are the subject of significant recent investigation.

2. EXPERIMENTAL SECTION

2.1. Synthesis. High-temperature solid-state methods were used to synthesize $TiNb_{24}O_{62}$. Stoichiometric masses of TiO_2 (Alfa-Aesar, 99.9%, anatase) and Nb_2O_5 (Sigma-Aldrich, 99.99%, mixed polymorphs) were thoroughly mixed with an agate mortar and pestle and cold pressed into 13 mm diameter × *ca*. 5 mm thick pellets (2–3 g) at 10 MPa. The pellets were then calcined at 1623 K for 96 h in platinum crucibles. The high-temperature niobia polymorph, monoclinic H-Nb_2O_5, was synthesized from thermal oxidation of NbO_2 in air at 1373 K for 24 h in an alumina crucible. The phase purity of this compound was determined via Rietveld refinement in a previous investigation of Nb_2O_5 polymorphism.[20]

2.2. Laboratory X-ray Powder Diffraction. Laboratory X-ray diffraction data were collected on a Panalytical Empyrean diffractometer with a Cu X-ray source and Kβ filter. Patterns were recorded in Bragg–Brentano reflection geometry from 5–80° 2θ in steps of 0.017° 2θ.

2.3. High-resolution Neutron Powder Diffraction. High-resolution constant-wavelength (λ = 1.5483 Å) neutron powder diffraction data were collected from 5–150° 2θ on the SPODI[21] beamline at the Heinz Maier-Leibnitz Zentrum (MLZ) in Garching, Germany. $TiNb_{24}O_{62}$ (5 g) was placed in a vanadium can for neutron measurements. For further details of the beamline instrumentation and data reduction process, see Ref. 21. Rietveld refinement[22] was carried out in

GSAS-II[23]. The entire data range 5–150° 2θ was used for the refinement. The background was empirically fit with an 18 term Chebyshev polynomial and peak shapes were modeled with a pseudo-Voigt lineshape. Crystal structure visualization and structural metric calculations were performed within VESTA 3.0.[24]

2.4. Scanning Electron Microscopy. Electron micrographs were collected at 3 kV on a Verios 460 scanning electron microscope (SEM, FEI Corp.). Samples were prepared by dispersing a few milligrams of $TiNb_{24}O_{62}$ powder into ethanol and casting the dispersion on a copper-supported carbon grid.

2.5. Electrochemistry. Electrochemical cells of Li (99.9%, Sigma-Aldrich) || 1 M $LiPF_6$ in ethylene carbonate/dimethyl carbonate (EC:DMC; 1:1, v/v; Merck) || $TiNb_{24}O_{62}$ were constructed in an argon glovebox containing < 0.1 ppm H_2O and < 0.1 ppm O_2. All cells were configured in the 2032-size coin cell geometry with stainless steel components and a glass fiber (Whatman) separator. $TiNb_{24}O_{62}$ electrodes were made by mixing the active material, Super P carbon (Timcal) and Kynar polyvinylidene difluoride (PVDF, Arkema) in an 8:1:1 mass ratio with *N*-methyl-2-pyrrolidone (NMP, Sigma-Aldrich, 99.5%, anhydrous), casting the resulting slurry onto aluminum foil or carbon-coated aluminum foil with a 100 μm doctor blade, and drying the film overnight at 60 °C. Circular electrode disks (1.27 cm diameter, 1.27 cm^2 geometric surface area, 2–3 $mg \cdot cm^{-2}$ active material mass loading) were cut with a punch press. All electrochemical measurements were performed on a Bio-Logic potentiostat/galvanostat operating EC-Lab software. Galvanostatic charge/discharge data were numerically differentiated to give differential voltage curves. Galvanostatic intermittent titration experiments were

performed by applying a current pulse at C/10 rate equivalent to 1/20th theoretical capacity followed by a rest period of 12 h to allow the potential to relax toward thermodynamic equilibrium. Under these conditions, one discharge–charge cycle corresponds to *ca.* 500 h. The theoretical capacity for a one electron reduction from Ti^{4+} to Ti^{3+} and Nb^{5+} to Nb^{4+} is 204.9 $mA \cdot h \cdot g^{-1}$ based on the mass of $TiNb_{24}O_{62}$. The C-rate is thus defined as inverse hours required to reach theoretical capacity; thus, C/10 corresponds to 20.49 $mA \cdot g^{-1}$.

3. RESULTS AND DISCUSSION

Synthesis and Structural Refinement. Solid-state reaction of Nb_2O_5 and TiO_2 at 1623 K resulted in a phase-pure white powder of $TiNb_{24}O_{62}$. SEM images and the neutron powder diffraction pattern of $TiNb_{24}O_{62}$ are shown in Figure 1. The particles were irregular in shape but roughly equant with a diameter of *ca*. 5-15 μm with no visible porosity (Figure 1a).

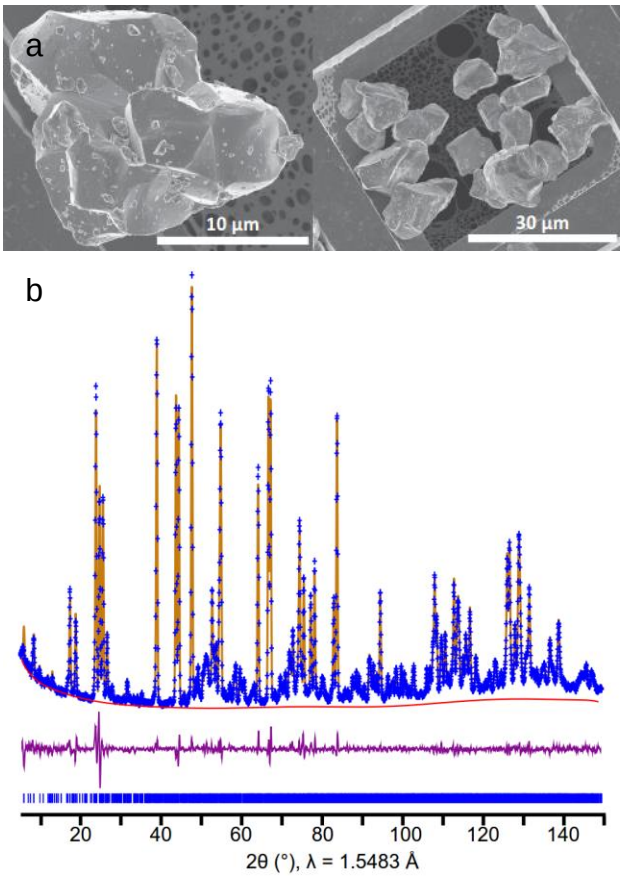

Figure 1. (a) SEM images and (b) results of Rietveld refinement of $TiNb_{24}O_{62}$ showing experimental data (blue crosses), model fit (orange curve), background fitted by Chebyshev polynomials (red curve), difference (purple curve), and calculated positions of Bragg peaks (vertical blue ticks).

Rietveld refinement[22] of the structural model against neutron scattering data (Figure 1b) was performed with GSAS-II[23]. The background, lattice parameters, atomic coordinates, atomic displacement parameters (ADPs), and metal site occupancies were initially refined in the *C*2 space group determined by Roth and Wadsley[13]. To reduce the large number of variables in this

large monoclinic structure, the ADPs were constrained to an overall value for all metal atoms and an overall value for all oxygen atoms. Interestingly, though no mirror symmetry is imposed in the initial space group choice, all octahedral metal sites and all oxygen sites refined well to the plane at $b = 0$. Given that (x, 0, z) is a site of mirror symmetry in $C2/m$, the remaining distinction between polar $C2$ and nonpolar $C2/m$ is the nature of the tetrahedral site, which could be ordered at (0, ¼, 0) or split occupancy above and below the b = ½ plane, as found in H-Nb_2O_5.[25] This difference was "beyond [the] immediate objective" of the initial structural characterization by Roth and Wadsley[13] and is therefore investigated here. Removing the mirror symmetry constraint and letting the atomic positions move off the plane at $b = 0$ increased the number of parameters in the least squares refinement by 43 but led to only a minor improvement in the fit from R_w = 5.945% to 5.703%. With all other atomic coordinates at (x, 0, z), converting the tetrahedral site from full occupancy at b = ¼ to a split position at b = ¼ and b = ¾ had almost no effect on the refinement and refining the occupancy of the two sites led to a 60:40 ratio. Thus, in the absence of significant evidence for symmetry lowering, the $C2/m$ space group was chosen though it is clear that the distinction is subtle in this compound. The possibility of small domains of lower symmetry cannot be excluded on the basis of diffraction data alone; observed deviations and non-50:50 split-site occupancy could be associated with complex domain structure in the material. Detailed transmission electron microscopy (TEM) imaging might be able to answer this question. The lattice parameters for the NPD refined structure (Figure 2) are a = 29.7940(4) Å, b = 3.82198(4) Å, c = 21.1301(4) Å, β = 95.043(3)° in close agreement with the original structure determination from XRD.

While the metal positions were accurately determined from XRD, the relatively weak scattering of x-rays from oxygen (Z = 8) vs. Ti (Z = 22) or Nb (Z = 41) prevented the determination of accurate or precise anion coordinates. Anomalous bond valence sums (BVS)[26] for Nb^{5+} and Ti^{4+} from the x-ray structure improved to within ± 10% for all sites after refinement of the neutron diffraction data: the mean BVS deviation was 11.4% before refinement and 4.9% after refinement (Supporting Information, Table S1). The most significant change was reflected in a 27% increase in polyhedral volume for the tetrahedral site with M–O bond lengths increasing from 1.644–1.730 Å to 1.82(2)–1.84(2) Å. Upon refining the metal site occupancies, preferential occupancy by titanium was found for the M1, M5, M8, M10, M11, and M13 sites, which are all edge-shared sites with the exception of M8 (Supporting Information, Table S2 & Figure S1). Ti occupancy refined to zero, within error, for all other sites and was thus fixed at zero for further refinements. In the related compounds $TiNb_2O_7$ and *o*-$Ti_2Nb_{10}O_{29}$, Cheetham and Von Dreele found analogous cation ordering preferences with titanium partially preferring (multiple) edge-sharing sites and niobium favoring sites at the center of the $n \times m$ blocks[18,19]. A study of the niobium–tungsten oxide $Nb_{14}W_3O_{44}$ yielded a similar finding, with W^{6+} preferring the center of the blocks and the lower valent Nb^{5+} in edge-sharing octahedra. No tetrahedral sites exist in either $TiNb_2O_7$ or

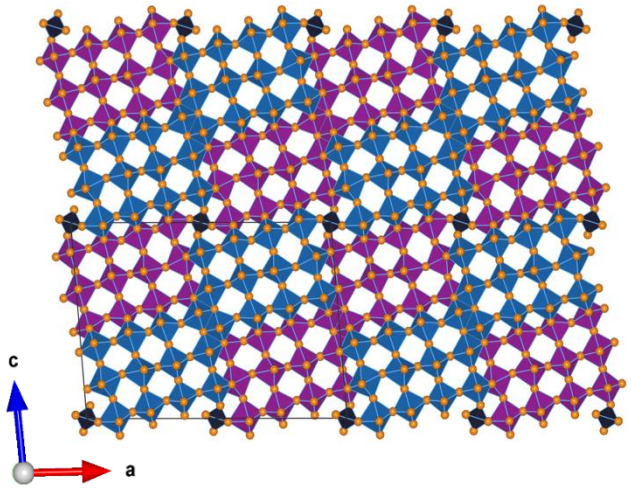

Figure 2. The 2 × 1 × 2 supercell of the crystallographic shear structure $TiNb_{24}O_{62}$ after NPD refinement. The $(3 \times 4)_2$ blocks of octahedra are clearly visible in this supercell view. The blocks in blue and purple are offset by ½ *b*. Tetrahedral sites are indicated with black shading. Oxygen ions are depicted as orange spheres. See main text for metal occupancies of the various sites and further structural details.

$Ti_2Nb_{10}O_{29}$; in the present study, the tetrahedral metal site in $TiNb_{24}O_{62}$ showed a preference for Ti^{4+} over the higher valent but equivalently sized Nb^{5+} ion. Without restraint, the total occupancy of niobium and titanium refined to 0.942 and 0.058, respectively, which are near the expected values of 0.96 and 0.04 so no restraint was imposed. During the Rietveld refinement all 31 oxygen sites were considered to be fully occupied and this parameter was not refined. Coordinates and occupancies for all 44 unique atomic positions are provided (Supporting Information, Table S2). Due to the second-order Jahn–Teller effect[27]—a symmetry-breaking structural displacement due to mixing of the ground-state filled p-orbitals with the pseudo-degenerate excited-state d-orbitals—in both d^0 Nb(V) and Ti(IV), the octahedra are highly distorted (Supporting Information, Table S1). The tetrahedral M1 site lacks a center of symmetry and is therefore not subject to this distortion.

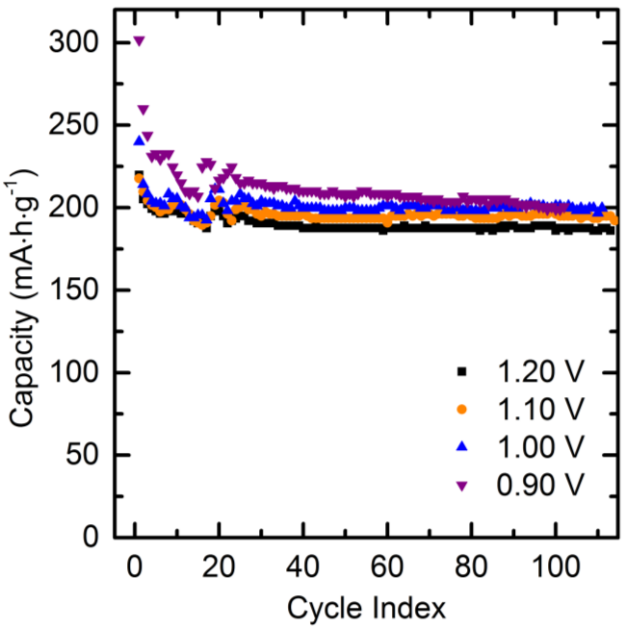

Figure 3. Cycle performance of $TiNb_{24}O_{62}$ from 3.0 V to 1.20 – 0.90 V vs. Li^+/Li for the first 100+ cycles at C/10. Undulations over the first 25 cycles result from temperature fluctuations.

Electrochemical Performance. In order to study the electrochemical performance of $TiNb_{24}O_{62}$ as a lithium-ion battery material, electrode films were prepared with conductive carbon and fluoropolymer binder (oxide:carbon:polymer 8:1:1 by mass). $TiNb_{24}O_{62}$ was cycled between 3.00 V and 1.20-0.90 V versus Li^+/Li at C/10. Figure 3 shows the cycling performance of this material as a function of lower voltage cutoff (V_{min}). On first discharge to 0.90 V,

$TiNb_{24}O_{62}$ intercalates 300 $mA \cdot h \cdot g^{-1}$ (1.5 Li/transition metal); however, there is a first cycle capacity loss of 40 $mA \cdot h \cdot g^{-1}$ and only 79% capacity retention from the 2nd to 100th cycle. Narrowing the potential window by raising the lower cutoff voltage stabilizes the capacity retention, as shown in Table 1. When the electrode was not taken below 1.10 V, the first cycle irreversible capacity was only *ca.* 4%. In addition, for electrodes that stayed above 1.00 V, the capacity retention over a three month time period from the 2nd to 100th cycle was 92-94%.

Lower Voltage Cutoff (V)	*1st Cycle Capacity ($mA \cdot h \cdot g^{-1}$)*	*1st Cycle Capacity Loss (%)*	*Capacity Retention (%) [2nd – 100th]*
0.90	302	15	79
1.00	240	11	93
1.10	218	3.7	94
1.20	214	4.1	92

Table 1. First cycle capacity, first cycle irreversible capacity, and capacity retention of $TiNb_{24}O_{62}$ vs. Li^+/Li as a function of the lower voltage cutoff.

As seen in Figure 4, the intercalation initially occurs primarily below 2.00 V with three reversible discharge regions. The first region exhibits a shoulder/slope from 2.05 V to 1.70 V and is *ca.* 40 $mA \cdot h \cdot g^{-1}$. Following this, intercalation is nearly potential invariant between 1.70-1.60 V for *ca.* 80 $mA \cdot h \cdot g^{-1}$. Finally, another sloping profile region occurs from 1.60 V to below 0.90 V with capacity dependent on cutoff voltage as discussed above. The full discharge and charge profiles are plotted for the 2nd, 10th, 50th, and 100th cycles as a function of lower voltage cutoff in Figure 4a. The high reversibility and extremely low overpotential (*ca.* 0.03 V on the

100th cycle from 3.00 to 1.20 V) are apparent when the voltage minimum is limited to 1.10 V. On the other hand, when cycled in a wider potential window, the cell polarization increases; a significant overpotential (*ca.* 0.80 V for the 100th cycle from 3.00 to 0.90 V) and lower energy efficiency are observed. Perhaps surprisingly, the capacity of the cells cycled to low voltage decays slowly (Figure 3) even whilst the polarization rises by more than a factor of 25 over the first 100 cycles. In other words, the energy efficiency is affected to a much greater extent than the capacity in this system, when the cells are cycled vs. Li (*i.e.*, when there is an excess of Li in the cell). The increase in polarization with cycle number suggests the build-up of a resistive SEI from electrolyte reduction at low potentials, which is consistent with the observation of irreversible capacity loss under low voltage cycling conditions.

Detailed analysis of the intercalation behavior is aided by the examination of *dQ/dV* plots shown

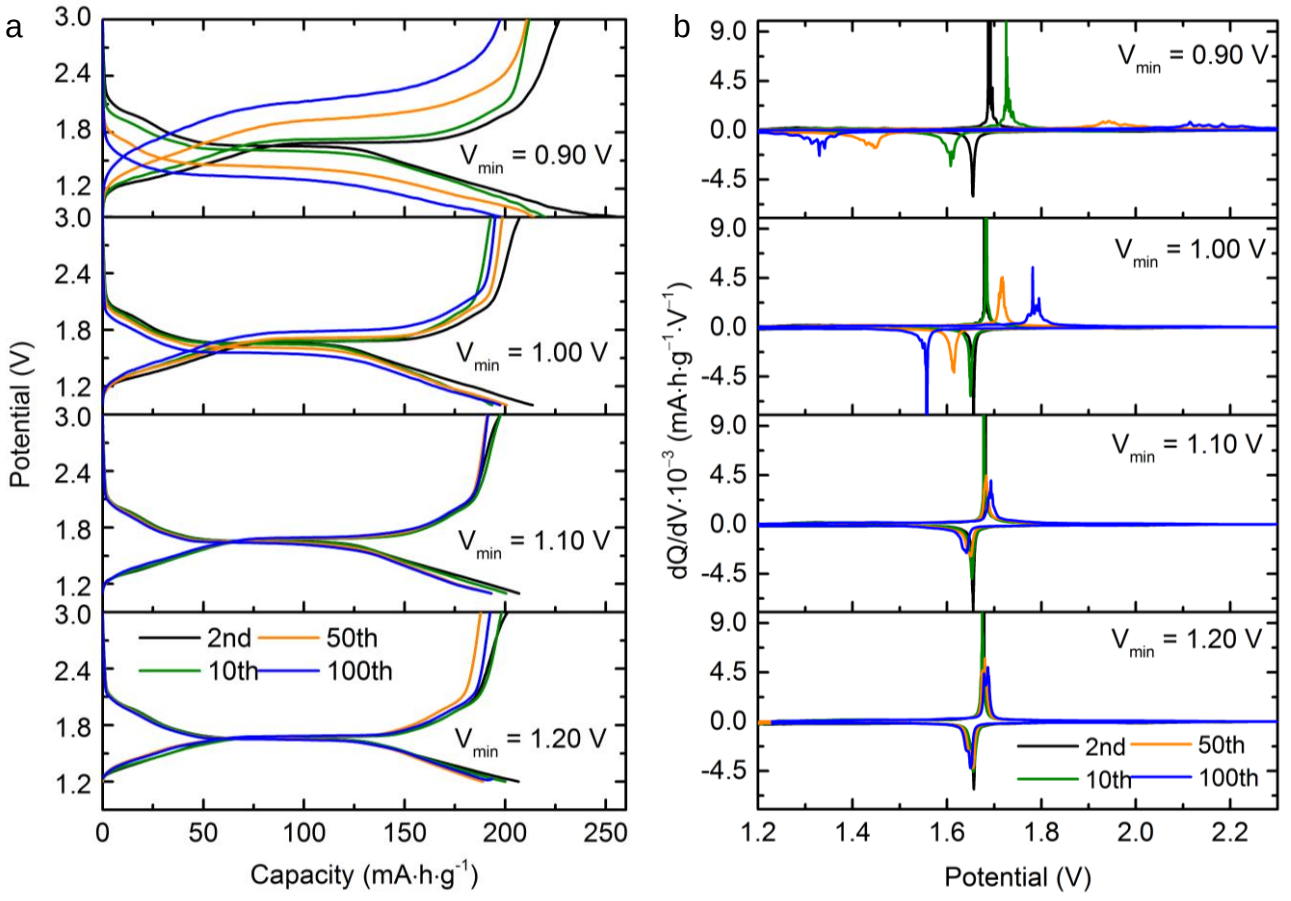

Figure 4. (a) Discharge and charge curves and (b) *dQ/dV* curves of $TiNb_{24}O_{62}$ as a function of minimum voltage limit (vs. Li^+/Li) and cycle number at C/10 rate. Expanded curves are given in Supplementary Figure S2.

in Figure 4b. Again, the 2nd, 10th, 50th, and 100th cycles are compared as a function of lower voltage cutoff. From Figure 4b, the decreasing peak potential on discharge (negative peaks) and increasing peak potential on charge (positive peaks) for low voltage cutoff cycling corresponds to the polarization seen in the curve separation from Figure 4a. In addition to the voltage shift, the *dQ/dV* reveals that the reduction and oxidation peaks broaden in all cases over cycling and even separate to distinct potentials for V_{min} of 1.00 V or below. Peak splitting in the *dQ/dV* suggests that the lithium sites are filling discretely and/or the particles are not being lithiated homogeneously after extended cycling to lower potentials. A view of the *dQ/dV* data with a smaller y-axis range is shown (Supporting Information, Figure S2) to highlight the effect of the sloping regions. The shoulder region at 2.00 V is present as a broad reversible peak in *dQ/dV* while the regions at higher and lower potential than the major redox peak show featureless intercalation on initial cycling and become overlapped with the broadened/split peaks on later cycles. The high degree of reversibility observed in cycling profiles and differential analysis (to 1.10 V) indicates that the crystal structure of $TiNb_{24}O_{62}$

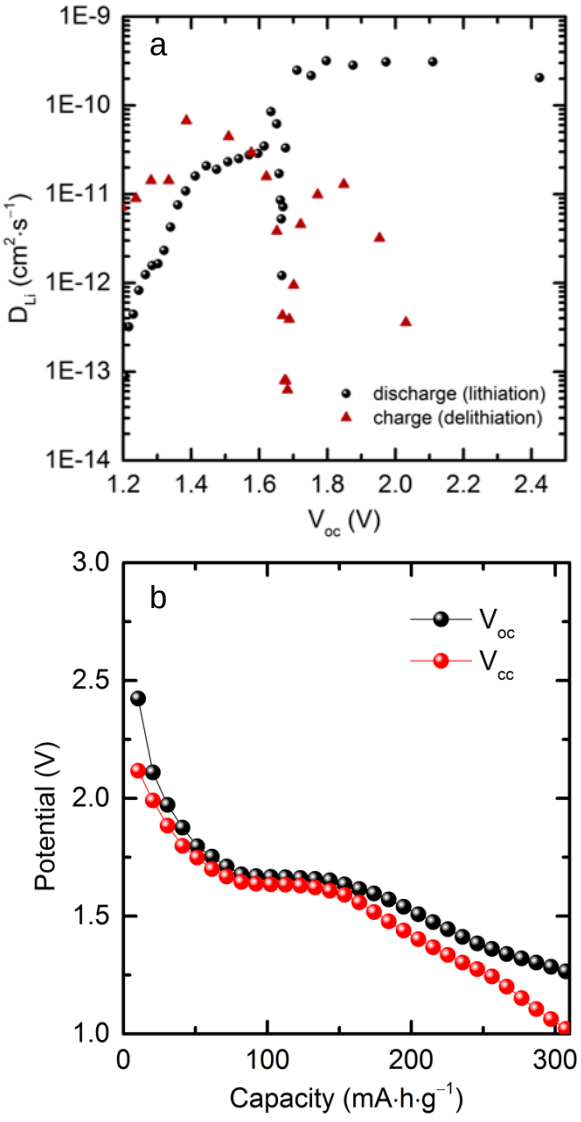

Figure 5. (a) $\widetilde{D}_{Li}$ as a function of open-circuit voltage and (b) the extracted open-circuit vs. closed-circuit plot from the first cycle at C/10 showing increased overpotential as $Li_xTiNb_{24}O_{62}$ surpasses x = 25 (1 Li^+/TM).

is very stable toward lithiation even over extended intercalation and deintercalation of a full formula unit of lithium.

The galvanostatic intermittent titration technique (GITT, Figure 5) was employed to gain insights into the (de)lithiation mechanism, diffusion kinetics, and thermodynamic voltage of $TiNb_{24}O_{62}$. In this experiment[28], a current pulse is applied followed by a long relaxation period and the cell voltage is continuously monitored (Supplementary Information, Figure S3). Immediately after the current pulse, the electrode is in a non-equilibrium state with a potential known as the closed-circuit voltage (V_{cc}). Throughout the relaxation period, Li^+ diffuses from the surface of the electrode/particles until it reaches an equilibrium state and corresponding open-circuit voltage (V_{oc}). As the observed voltage during the relaxation step is a function of a diffusive process, the chemical diffusion coefficient ($\widetilde{D}_{Li}$) can be derived[28]. While absolute values of $\widetilde{D}_{Li}$ from GITT of polycrystalline electrodes are susceptible to errors in the estimation of particle size/diffusion distance, relative values are quite informative. During the initial lithiation, $\widetilde{D}_{Li}$ is relatively constant from 2.45 V until the divergent behavior at 1.68 V. The divergent region corresponds to a stoichiometry of $Li_{8.5(1.0)}TiNb_{24}O_{62}$—close to the one-third lithiated composition $Li_{8.33}TiNb_{24}O_{62}$—to $Li_{20(1)}TiNb_{24}O_{62}$ and suggests a two-phase reaction or region of lithium-ordering. Intermittent titration technique diffusion coefficients, based on Fickian diffusion, are only applicable within single-phase regions[28,29] and thus the phenomenon, not the absolute values, should be regarded for this divergent region.[30] Efforts have been made to extend GITT theory to phase transformation regions by accounting for the interface mobility but further knowledge or assumptions are required concerning the particle size, morphology, and distribution as well as the geometry of intercalant diffusion and interface propagation.[31] Upon

lithiation below an open-circuit voltage of *ca.* 1.6 V, from $Li_{20(1)}TiNb_{24}O_{62}$ to $Li_{27.5(1.0)}TiNb_{24}O_{62}$, Li^+ diffusion enters a second relatively constant region that is one order-of-magnitude lower than the dilute $Li_xTiNb_{24}O_{62}$ to $Li_{8.5(1.0)}TiNb_{24}O_{62}$ region. Finally, from $Li_{27.5(1.0)}TiNb_{24}O_{62}$ to $Li_{37.5(1.0)}TiNb_{24}O_{62}$, the Li^+ diffusion becomes steadily more hindered. This could be attributed to filling of the sites as the phase becomes overlithiated, *i.e.* greater than one lithium per transition metal (Li^+/TM). While this "lithium-stuffed" phase can incorporate additional Li-ions, the diffusion is slower (Figure 5a). Overall, Li^+ diffusion decreases by 10^3 from dilute $Li_xTiNb_{24}O_{62}$ to stuffed $Li_{37.5(1.0)}TiNb_{24}O_{62}$. In addition, the difference between V_{oc} and V_{cc} increases from 45 mV at 0.75 Li^+/TM to 105 mV at 1.0 Li^+/TM to 244 mV at 1.5 Li^+/TM (Figure 5b). The low hysteresis between discharge and charge, particularly above V_{cc} = 1.2 V, demonstrates the energy efficiency of $TiNb_{24}O_{62}$. Accessing higher capacities, at least in these bulk particles, is possible under "thermodynamic conditions" as in GITT or slow cycling but will incur some efficiency and stability penalties.

The rate performance of $TiNb_{24}O_{62}$ was examined with thick films (2–3 mg·cm^{-2} active material) prepared from the *ca.* 5–15 μm particles (Figure 6, Supplementary Figure S4). On aluminum foil current collectors, the $TiNb_{24}O_{62}$ capacity faded as a function of increasing current density with approximately 50% capacity realized at 2C (409.8 mA·g^{-1}) and nearly no charge storage above 5C (1025 mA·g^{-1}) in a standard 2032-size coin cell with one 0.5 mm stainless steel spacer disk and a 1.0 mm conical spring. It is known that pressure can play a role in cell performance so cells were also examined with a second 0.5 mm spacer disk added; this significantly improved the high-rate performance such that 50% theoretical capacity was achieved at 5C. Given that theoretical capacity was reached at C/5, this phase might be considered a typical battery material

for standard rate conditions. Still, in order to better understand the nature of the rate limitations, $TiNb_{24}O_{62}$ was also cast onto carbon-coated Al foil (C@Al), (Figure 6, Supplementary Figure S4), it being a well-established method in the carbon supercapacitor community to produce electric double-layer supercapacitors with current densities in the range 1–100 $mA \cdot cm^{-2}$.[32,33] In this study, thick films comprised of the large particles of $TiNb_{24}O_{62}$ maintained greater than 50% theoretical capacity at 10–15C (2–3 $A \cdot g^{-1}$; 6.7–10 $mA \cdot cm^{-2}$). These results suggest that this phase is not only stable upon long-term cycling but also has intrinsic high-rate insertion and extraction of lithium under appropriate conditions, which is reminiscent of the bronze-phase T-Nb_2O_5[20]. We note that pressure and a constant voltage charge step (involving a 1 hour hold period at 3.0 V) appear to be much more significant on the non-optimized Al foil whilst having little effect on the performance of $TiNb_{24}O_{62}$ on a more suitable substrate such as carbon-coated Al foil. The lack of effect of a one hour hold period for the carbon-coated films indicates that the measured capacities reflect the intrinsic behavior of the oxide film on discharge and that $TiNb_{24}O_{62}$ is not limited by the ability to extract Li^+ on charge. The results are consistent with rapid Li^+ transport in the oxide, despite the drop in the lithium diffusivity with increasing lithium content.

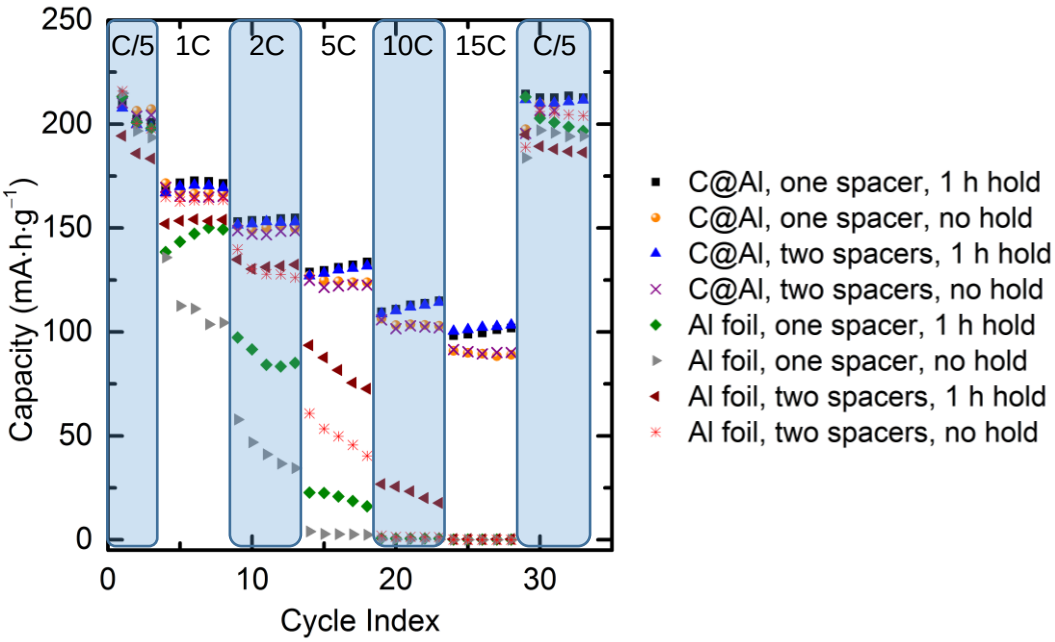

Figure 6. High-rate performance of $TiNb_{24}O_{62}$ vs. Li. The mixed metal oxide capacity was examined as a function of current collector substrate, pressure, and cycling conditions in a 3.0–1.0 V potential window (vs. Li^+/Li): capacity data are displayed for (i) carbon-coated Al foil (C@Al) and untreated Al foil, (ii) one or two 0.5 mm stainless steel spacer disks, and (iii) with or without a 1 h constant voltage hold step at the top of charge (3.0 V). Electrodes were 1.27 cm in diameter, the active material mass loading was 3–4 mg, and the composition was $TiNb_{24}O_{62}$:carbon:PVDF in 8:1:1 mass ratio, analogous to the long duration cycling.

Comparison with Related Structure Types. With the goal of understanding and designing next-generation energy storage materials, it is interesting to consider how the block superstructure changes with minimal compositional differences and how the block size and interconnectivity may affect properties such as intercalation chemistry. The difference between $TiNb_{24}O_{62}$ $(3 \times 4)_2$ and the block structures found in H-Nb_2O_5[25] $[(3 \times 4)_1+(3 \times 5)_\infty]$, *i.e.*, $Nb_{25}O_{62.5}$, is the absence of only one out of every 125 oxygen atoms. Rather than a disordered defect, this minor change in anion stoichiometry, dictated by charge neutrality, results in an ordered shear structure with a different block connectivity and thus different ionic diffusion pathways. This structural rearrangement is also observed in the case of α-$ZrNb_{24}O_{62}$[34], which is isostructural with $TiNb_{24}O_{62}$. In the case of Zr, however, two additional polymorphs are known from electron microscopy—β and γ—though they are not fully characterized due to the

complexity of their crystal structures.[34] These additional polymorphs are observed after prolonged heating of Nb_2O_5 and ZrO_2, which yields primarily α-phase after *ca.* 24 h and primarily β-phase after *ca.* 160 h. In an effort to investigate the stability of $TiNb_{24}O_{62}$, a sample was heated in a Pt crucible in air at 1623 K for 166.5 h followed by 1673 K for a further 166.5 h. No apparent phase transformation was observed in the powder X-ray diffraction data though the weak, high d-spacing superstructure reflections became more pronounced after extended annealing (Supplementary Figure S5).

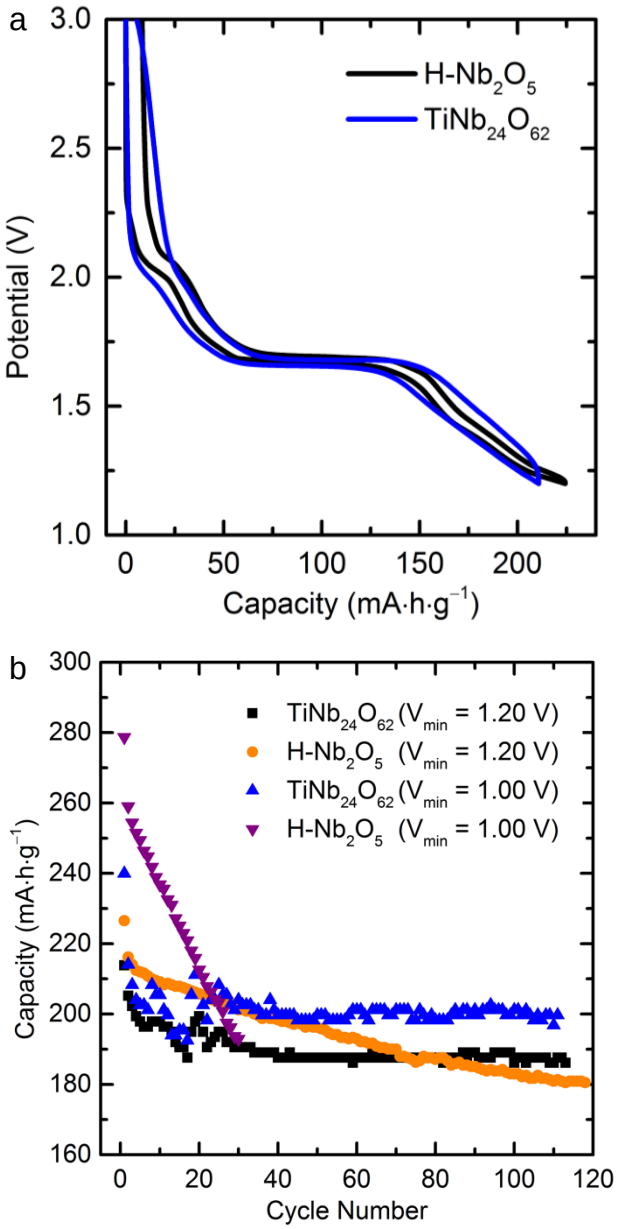

Figure 7. Comparison of the electrochemical properties of $TiNb_{24}O_{62}$ and H-Nb_2O_5. (a) 2nd cycle lithiation/delithiation profiles and (b) capacity as a function of compound, cycle number, and lower voltage cut-off. All tests were performed at C/10 rate in coin cells with additive-free 1 M $LiPF_6$ in EC:DMC (1:1, v/v) and an upper voltage limit of 3.0 V.

As aforementioned, the monoclinic H-Nb_2O_5 *cs* phase is compositionally and structurally closely related to $TiNb_{24}O_{62}$. While the discharge and charge processes are similar in reaction voltage and capacity between the two phases, the shoulder regions from 0–0.25, 0.70–1.00, and beyond one Li^+/TM are significantly suppressed and smoothed out in $TiNb_{24}O_{62}$, appearing more solid-solution-like (Figure 7a). This may be related to the presence of disordered cation sublattices containing Nb and Ti ions with different charges, which

can help prevent Li^+ ordering, although at such low Ti concentrations the effects are clearly subtle. Given their structural and compositional similarity, it is noteworthy that under the same conditions—rate, particle size, voltage window, temperature, electrolyte, and cell design—the capacity retention of $TiNb_{24}O_{62}$ is significantly higher and more stable than H-Nb_2O_5 (Figure 7b). Both structures feature (*3* × *4*) blocks and tetrahedral linkages though every other ½ *b* layer in H-Nb_2O_5 is comprised of an infinite chain of (*3* × *5*) blocks. While it is difficult to pinpoint the exact nature of the difference in capacity retention in these complex structures, the specific arrangement of the shear planes, block sizes, and block connectivity certainly has implications for electrochemical performance in the extended family of *cs* phases.

Structural and Property Comparisons within the Nb–Ti–O Phase Diagram. Given the substantial and rising interest in Ti- and Nb-containing electrode materials for energy storage[6,8,9,20,35], the Nb–Ti–O phase space is as important as it is complex. We seek to bring together ideas from the previous structural studies and phase chemistry in this context. As introduced, $TiNb_2O_7$, *m*-$Ti_2Nb_{10}O_{29}$, *o*-$Ti_2Nb_{10}O_{29}$, and intergrowth phases are well known. Recently, Lin *et al.*[36] suggested the existence of another electrode material with the stoichiometry $TiNb_6O_{17}$ ($TiO_2{\cdot}3Nb_2O_5$) and proposed that the structure is similar to that of monoclinic-$Ti_2Nb_{10}O_{29}$ but that it contained cation vacancies. Roth and Coughanour[37] reported this phase in the titania–niobium system sixty years prior but recognized that the formula was uncertain; in a subsequent single-crystal X-ray study, Wadsley[38] reported that reaction with a 1:3 TiO_2:Nb_2O_5 stoichiometry also yielded H-Nb_2O_5 and showed that the proposed "1:3" phase was actually $2TiO_2{\cdot}5Nb_2O_5$. The recent proposal that $TiNb_6O_{17}$ is a new phase, based on its composition, but with a good fit to the diffraction pattern of *m*-$Ti_2Nb_{10}O_{29}$[36] requires significant further evidence if

one considers (i) the previous single-crystal work by Wadsley, (ii) the lack of evidence for this cation-deficient defect motif in other *cs* structures, (iii) the infinitely adaptive nature of the cs structures, especially given the similar block sizes of H-Nb_2O_5 and $Ti_2Nb_{10}O_{29}$, and (iv) the difficulty of detecting a small percentage of microheterogeneous regions with laboratory X-ray diffraction (employed in the prior study) amongst the already complex diffraction pattern. Indeed, coherent intergrowths of domains as small as a single block-width are known in the TiO_2–Nb_2O_5 system.[39] A thorough TEM investigation and careful pycnometry measurements may help resolve this section of the phase diagram; however, for the reasons discussed, $TiNb_6O_{17}$ is omitted at present. Finally, the phase $Ti_2Nb_6O_{19}$ may exist, which Jongejan and Wilkins reported to be stable only above 1425 °C, but has not been structurally characterized.[40] Therefore, the updated TiO_2–Nb_2O_5 phase diagram (Figure 8), based on the diagram from Roth,[41] now clarifies the polymorphism in $Ti_2Nb_{10}O_{29}$, the lack thereof in $TiNb_{24}O_{62}$, intergrowths of ternary phases with H-Nb_2O_5, and the consideration of other stoichiometries, which require further investigation.

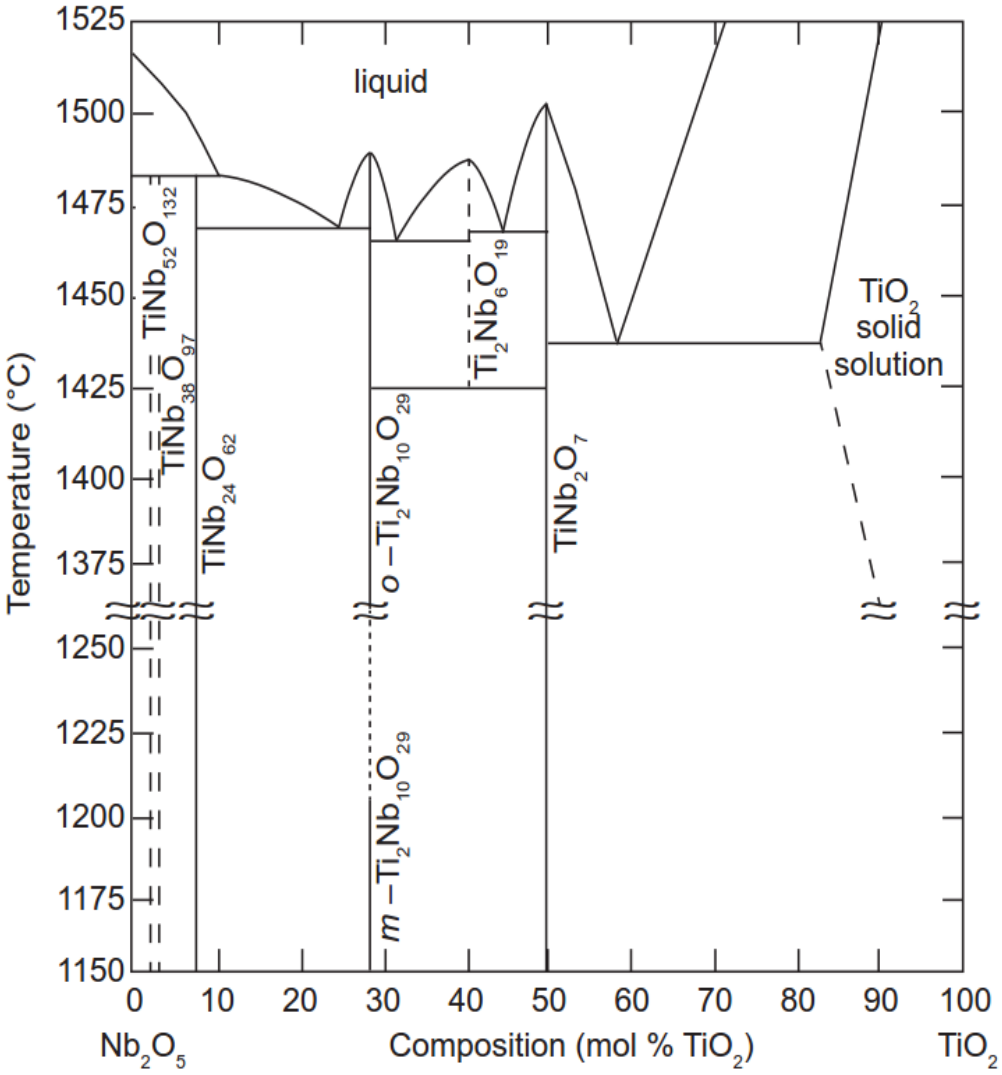

Figure 8. Temperature versus composition phase diagram of the Nb_2O_5–TiO_2 system at ambient pressure. Nb_2O_5, $TiNb_{24}O_{62}$, $Ti_2Nb_{10}O_{29}$, $TiNb_2O_7$, a solid-solution of Nb in TiO_2, and TiO_2 are well established. $Ti_2Nb_{10}O_{29}$ is found as monoclinic (*m*) and orthorhombic (*o*) polymorphs. Nb solubility in TiO_2 decreases as a function of temperature below 1475 °C. Ti solubility in Nb_2O_5 is minimal. Dashed vertical lines indicate regions where structures are not well defined and/or T–C space is not well sampled.[15] Phase data based on Roth[41] and supplemented from the literature[14-17,40] and this work.

Electrochemical studies of $TiNb_2O_7$[6,42] and $Ti_2Nb_{10}O_{29}$[9,10,43] have reported good capacity and cycling performance, especially when steps were taken to reduce the particle size or improve the electrode design[44–46]. This report on $TiNb_{24}O_{62}$ is comparable with other members of the same family; bulk $TiNb_2O_7$[7,42,47] and $Ti_2Nb_{10}O_{29}$[10] were reported to cycle 200–250 $mA{\cdot}h{\cdot}g^{-1}$ though

most studies report just the first 20 cycles and use smaller particles. Thus, the intercalation reversibility of $TiNb_{24}O_{62}$ is comparable to other safe anode candidates while further studies are needed to differentiate this family of electrode materials. Furthermore, though it is known that the gassing in $Li_4Ti_5O_{12}$ is more detrimental than in TiO_2[1], the role of titanium in this process is not yet clear. This Nb-rich end member of the family of Ti–Nb–O compounds may help with the identification of the mechanism of gassing and prove useful if gassing is indeed tied to Ti-rich interface chemistry. The advanced synthetic techniques applied to $TiNb_2O_7$ or $Ti_2Nb_{10}O_{29}$ to carbon coat[42], introduce charge carriers through partial reduction[48], or nanoscale the particles[44–46,49] may be analogously applied to increase the capacity and kinetics of $TiNb_{24}O_{62}$.

4. CONCLUSIONS

A titanium–niobium mixed metal oxide in the Wadsley–Roth family of crystallographic shear compounds has been structurally and electrochemically characterized. Neutron diffraction was applied for the first time to $TiNb_{24}O_{62}$ to elucidate subtle structural details. Thanks to the scattering properties of neutrons, the oxygen bonding was more accurately derived and partial cation ordering was found with Ti^{4+} preferentially occupying the tetrahedral site and some multi-edge-sharing octahedra within $TiNb_{24}O_{62}$. In this complex oxide, intercalation and deintercalation occur in three broad regions between 2.0 and 1.2–0.9 V with a reversible capacity of *ca.* 190 $mA{\cdot}h{\cdot}g^{-1}$ over 100 cycles (three month period) in dense electrodes of *ca.* 10 μm particles. Long-term cycling to lower potentials (at or below 1.0 V) results in polarization and separation of the average and individual redox peaks. In a slightly narrower potential window, the first-cycle irreversibility can be mitigated and long-term capacity retention maintained. GITT measurements revealed differential lithium-ion mobility, which could be partitioned into

four regions of composition, and showed that "lithium-stuffing" rapidly reduces diffusion within the structure. In the absence of overlithiation, rapid Li^+ diffusion in the bulk is evidently present within the shear structure of $TiN_{24}O_{62}$ as high-rate electrochemical testing demonstrated a reversible capacity of 150 $mA{\cdot}h{\cdot}g^{-1}$ in *ca.* 20 mins and 100 $mA{\cdot}h{\cdot}g^{-1}$ in *ca.* 2 mins. The high-rate cycling also revealed a sensitivity of this material structure/morphology to the current collector substrate and, to a lesser extent, pressure and charging conditions. The phase chemistry of TiO_2–Nb_2O_5 was discussed and an updated phase diagram presented to facilitate the development of this promising family of energy storage materials. Future studies on electrolyte decomposition/gassing and the effects of advanced synthetic and/or post-synthetic treatments will yield further insight into the applicability of this material as a high-capacity, safe anode material. Computational quantum or classical dynamics calculations could reveal the role of cation ordering and differences in local diffusion around titanium and niobium.

ASSOCIATED CONTENT

Supporting Information Available: CIF file, tabular structural data, tabular bond valence sums and distortion analysis, crystal structure model highlighting Ti-enriched sites, expanded *dQ/dV* plots, GITT pulse response, electrochemical discharge profiles at high current densities, and XRD as a function of annealing time. Data supporting this work are available from www.repository.cam.ac.uk.

AUTHOR INFORMATION

Corresponding Author

*cpg27@cam.ac.uk

Notes

The authors declare no competing financial interest.

ACKNOWLEDGMENTS

The assistance of Dr. Martin J. Mühlbauer with neutron measurements and discussions with Dr. Matthew J. Cliffe regarding crystallography are sincerely appreciated. In addition, the authors gratefully acknowledge the financial support provided by FRM II to perform the neutron scattering measurements at the Heinz Maier-Leibnitz Zentrum (MLZ), Garching, Germany. The authors thank Dr. Melanie Loveridge, University of Warwick for providing current collector substrates. K.J.G. thanks the Winston Churchill Foundation of the United States and the Herchel Smith Scholarship for funding.

REFERENCES

(1) He, Y.-B.; Li, B.; Liu, M.; Zhang, C.; Lv, W.; Yang, C.; Li, J.; Du, H.; Zhang, B.; Yang, Q.-H.; Kim, J.-K.; Kang, F. Gassing in $Li_4Ti_5O_{12}$-Based Batteries and Its Remedy. *Sci. Rep.* **2012**, *2*, 913.

(2) Cava, R. J.; Murphy, D. W.; Zahurak, S. M. Lithium Insertion in Wadsley-Roth Phases Based on Niobium Oxide. *J. Electrochem. Soc.* **1983**, *130*, 2345–2351.

(3) Kumagai, N.; Koishikawa, Y.; Komaba, S.; Koshiba, N. Thermodynamics and Kinetics of Lithium Intercalation into Nb_2O_5 Electrodes for a 2 V Rechargeable Lithium Battery. *J. Electrochem. Soc.* **1999**, *146*, 3203–3210.

(4) Kim, J. W.; Augustyn, V.; Dunn, B. The Effect of Crystallinity on the Rapid Pseudocapacitive Response of Nb_2O_5. *Adv. Energy Mater.* **2012**, *2*, 141–148.

(5) Catti, M.; Ghaani, M. R. On the Lithiation Reaction of Niobium Oxide: Structural and Electronic Properties of $Li_{1.714}Nb_2O_5$. *Phys. Chem. Chem. Phys.* **2014**, *16*, 1385–1392.

(6) Han, J.-T.; Goodenough, J. B. 3-V Full Cell Performance of Anode Framework $TiNb_2O_7$/Spinel $LiNi_{0.5}Mn_{1.5}O_4$. *Chem. Mater.* **2011**, *23*, 3404–3407.

(7) Lu, X.; Jian, Z.; Fang, Z.; Gu, L.; Hu, Y.-S.; Chen, W.; Wang, Z.; Chen, L. Atomic-Scale Investigation on Lithium Storage Mechanism in $TiNb_2O_7$. *Energy Environ. Sci.* **2011**, *4*, 2638–2644.

(8) Guo, B.; Yu, X.; Sun, X.-G.; Chi, M.; Qiao, Z.-A.; Liu, J.; Hu, Y.-S.; Yang, X.-Q.; Goodenough, J. B.; Dai, S. A Long-Life Lithium-Ion Battery with a Highly Porous $TiNb_2O_7$ Anode for Large-Scale Electrical Energy Storage. *Energy Environ. Sci.* **2014**, *7*, 2220–2226.

(9) Wu, X.; Miao, J.; Han, W.; Hu, Y.-S.; Chen, D.; Lee, J.-S.; Kim, J.; Chen, L. Investigation on $Ti_2Nb_{10}O_{29}$ Anode Material for Lithium-Ion Batteries. *Electrochem. Commun.* **2012**, *25*, 39–42.

(10) Cheng, Q.; Liang, J.; Zhu, Y.; Si, L.; Guo, C.; Qian, Y. Bulk $Ti_2Nb_{10}O_{29}$ as Long-Life and High-Power Li-Ion Battery Anodes. *J. Mater. Chem. A* **2014**.

(11) Kunz, M.; Brown, I. D. Out-of-Center Distortions around Octahedrally Coordinated d^0 Transition Metals. *J. Solid State Chem.* **1995**, *115*, 395–406.

(12) Andersson, S.; Wadsley, A. D. Crystallographic Shear and Diffusion Paths in Certain Higher Oxides of Niobium, Tungsten, Molybdenum and Titanium. *Nature* **1966**, *211*, 581–583.

(13) Roth, R. S.; Wadsley, A. D. Mixed Oxides of Titanium and Niobium: The Crystal Structure of $TiNb_{24}O_{62}$ ($TiO_2 \cdot 12Nb_2O_5$). *Acta Crystallogr.* **1965**, *18*, 724–730.

(14) Yamaguchi, O.; Tomihisa, D.; Ogiso, N.; Shimizu, K. Crystallization of Monoclinic $2TiO_2 \cdot 5Nb_2O_5$. *J. Am. Ceram. Soc.* **1986**, *69*, C-150.

(15) Allpress, J. G. Mixed Oxides of Titanium and Niobium: Intergrowth Structures and Defects. *J. Solid State Chem.* **1969**, *1*, 66–81.

(16) Allpress, J. G. Mixed Oxides of Titanium and Niobium: Defects in Quenched Samples. *J. Solid State Chem.* **1970**, *2*, 78–93.

(17) *Perspectives in Structural Chemistry*; Dunitz, J. D., Ibers, J. A., Eds.; John Wiley & Sons, Inc., 1970; Vol. III.

(18) Cheetham, A. K.; Dreele, V.; B, R. Cation Distributions in Niobium Oxide Block Structures. *Nature* **1973**, *244*, 139–140.

(19) Dreele, R. B. V.; Cheetham, A. K. The Structures of Some Titanium-Niobium Oxides by Powder Neutron Diffraction. *Proc. R. Soc. Lond. Math. Phys. Sci.* **1974**, *338*, 311–326.

(20) Griffith, K. J.; Forse, A. C.; Griffin, J. M.; Grey, C. P. High-Rate Intercalation without Nanostructuring in Metastable Nb_2O_5 Bronze Phases. *J. Am. Chem. Soc.* **2016**, *138*, 8888–8899.

(21) Hoelzel, M.; Senyshyn, A.; Juenke, N.; Boysen, H.; Schmahl, W.; Fuess, H. High-Resolution Neutron Powder Diffractometer SPODI at Research Reactor FRM II. *Nucl. Instrum. Methods Phys. Res. Sect. Accel. Spectrometers Detect. Assoc. Equip.* **2012**, *667*, 32–37.

(22) Rietveld, H. M. A Profile Refinement Method for Nuclear and Magnetic Structures. *J. Appl. Crystallogr.* **1969**, *2*, 65–71.

(23) Toby, B. H.; Von Dreele, R. B. *GSAS-II* : The Genesis of a Modern Open-Source All Purpose Crystallography Software Package. *J. Appl. Crystallogr.* **2013**, *46*, 544–549.
(24) Momma, K.; Izumi, F. *VESTA 3* for Three-Dimensional Visualization of Crystal, Volumetric and Morphology Data. *J. Appl. Crystallogr.* **2011**, *44*, 1272–1276.
(25) Kato, K. Structure Refinement of H-Nb_2O_5. *Acta Crystallogr. B* **1976**, *32*, 764–767.
(26) Brown, I. D. *The Chemical Bond in Inorganic Chemistry: The Bond Valence Model*; Oxford University Press, 2002.
(27) Opik, U.; Pryce, M. H. L. Studies of the Jahn–Teller Effect. I. A Survey of the Static Problem. *Proc. R. Soc. Lond. Ser. Math. Phys. Sci.* **1957**, *238*, 425–447.
(28) Weppner, W.; Huggins, R. A. Determination of the Kinetic Parameters of Mixed-Conducting Electrodes and Application to the System Li_3Sb. *J. Electrochem. Soc.* **1977**, *124*, 1569–1578.
(29) Wen, C. J.; Boukamp, B. A.; Huggins, R. A.; Weppner, W. Thermodynamic and Mass Transport Properties of " LiAl ." *J. Electrochem. Soc.* **1979**, *126*, 2258–2266.
(30) Shu, G. J.; Chou, F. C. Sodium-Ion Diffusion and Ordering in Single-Crystal P2-Na_xCoO_2. *Phys Rev B* **2008**, *78*, 052101.
(31) Zhu, Y.; Wang, C. Galvanostatic Intermittent Titration Technique for Phase-Transformation Electrodes. *J. Phys. Chem. C* **2010**, *114*, 2830–2841.
(32) Portet, C; Taberna, P.-L.; Simon, P.; Laberty-Robert, C. Modification of Al Current Collector Surface by Sol–Gel Deposit for Carbon–Carbon Supercapacitor Applications. *Electrochim. Acta* **2004**, *49*, 905–912.
(33) Portet, C; Taberna, P.-L.; Simon, P.; Flahaut, E.; Laberty-Robert, C. High Power Density Electrodes for Carbon Supercapacitor Applications. *Electrochim. Acta* **2005**, *50*, 4174–4181.
(34) Allpress, J. G.; Roth, R. S. Structural Studies by Electron Microscopy: Polymorphism of $ZrO_2 \cdot 12Nb_2O_5$. *J. Solid State Chem.* **1970**, *2*, 366–376.
(35) Armstrong, A. R.; Armstrong, G.; Canales, J.; García, R.; Bruce, P. G. Lithium-Ion Intercalation into TiO_2-B Nanowires. *Adv. Mater.* **2005**, *17*, 862–865.
(36) Lin, C.; Wang, G.; Lin, S.; Li, J.; Lu, L. $TiNb_6O_{17}$: A New Electrode Material for Lithium-Ion Batteries. *Chem. Commun.* **2015**, *51*, 8970–8973.
(37) Roth, R. S.; Coughanour, L. W. Phase Equilibrium Relations in the Systems Titania-Niobia and Zirconia-Niobia. *J. Res. Natl. Bur. Stand.* **1955**, *55*, 209.
(38) Wadsley, A. D. Mixed Oxides of Titanium and Niobium. II. The Crystal Structures of the Dimorphic Forms $Ti_2Nb_{10}O_{29}$. *Acta Crystallogr.* **1961**, *14*, 664–670.
(39) Forghany, S. K. E.; Cheetham, A. K.; Olsen, A. X-Ray Microanalysis and High-Resolution Transmission Electron Microscopy of the Reduced Titanium-Niobium Oxides. *J. Solid State Chem.* **1987**, *71*, 305–323.
(40) Jongejan, A.; Wilkins, A. L. A Re-Examination of the System Nb_2O_5-TiO_2 at Liquidus Temperatures. *J. Common Met.* **1969**, *19*, 185–191.
(41) Roth, R. S. Thermal Stability of Long Range Order in Oxides. *Prog. Solid State Chem.* **1980**, *13*, 159–192.
(42) Han, J.-T.; Huang, Y.-H.; Goodenough, J. B. New Anode Framework for Rechargeable Lithium Batteries. *Chem. Mater.* **2011**, *23*, 2027–2029.
(43) Takashima, T.; Tojo, T.; Inada, R.; Sakurai, Y. Characterization of Mixed Titanium–Niobium Oxide $Ti_2Nb_{10}O_{29}$ Annealed in Vacuum as Anode Material for Lithium-Ion Battery. *J. Power Sources* **2015**, *276*, 113–119.
(44) Cheng, Q.; Liang, J.; Lin, N.; Guo, C.; Zhu, Y.; Qian, Y. Porous $TiNb_2O_7$ Nanospheres as Ultra Long-Life and High-Power Anodes for Lithium-Ion Batteries. *Electrochimica Acta*. **2015**, *176*, 456-462.
(45) Lou, S.; Ma, Y.; Cheng, X.; Gao, J.; Gao, Y.; Zuo, P.; Du, C.; Yin, G. Facile Synthesis of Nanostructured $TiNb_2O_7$ Anode Materials with Superior Performance for High-Rate Lithium Ion Batteries. *Chem. Commun.* **2015**, *51*, 17293-17296.

(46) Tang, K.; Mu, X.; van Aken, P. A.; Yu, Y.; Maier, J. "Nano-Pearl-String" $TiNb_2O_7$ as Anodes for Rechargeable Lithium Batteries. *Adv. Energy Mater.* **2013**, *3*, 49–53.
(47) Saritha, D.; Varadaraju, U. V. Studies on Electrochemical Lithium Insertion in Isostructural Titanium Niobate and Tantalate Phases with Shear ReO_3 Structure. *Mater. Res. Bull.* **2013**, *48*, 2702–2706.
(48) Lin, C.; Yu, S.; Zhao, H.; Wu, S.; Wang, G.; Yu, L.; Li, Y.; Zhu, Z.-Z.; Li, J.; Lin, S. Defective $Ti_2Nb_{10}O_{27.1}$: An Advanced Anode Material for Lithium-Ion Batteries. *Sci. Rep.* **2015**, *5*, 17836.
(49) Li, H.; Shen, L.; Pang, G.; Fang, S.; Luo, H.; Yang, K.; Zhang, X. $TiNb_2O_7$ Nanoparticles Assembled into Hierarchical Microspheres as High-Rate Capability and Long-Cycle-Life Anode Materials for Lithium Ion Batteries. *Nanoscale* **2014**, *7*, 619–624.

For Table of Contents Only

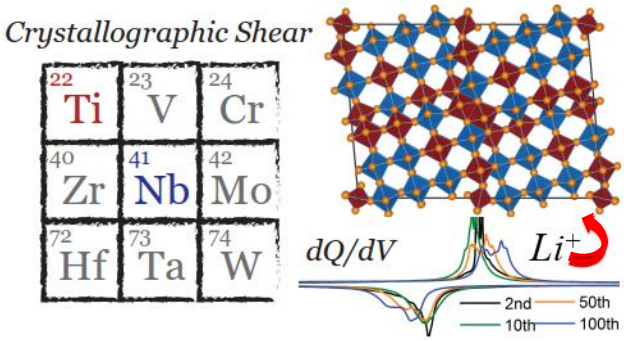

$TiNb_{24}O_{62}$ is a crystallographic shear structure with (*3* × *4*) blocks of octahedra joined by shear planes and tetrahedral sites. Neutron diffraction shows a preference for selective titanium occupancy and highly distorted MO_6 octahedra. Electrochemical measurements against lithium reveal reversible intercalation, high-rate performance in the bulk, and the role of "lithium-stuffing" on ion dynamics within the block structure. Compounds in the TiO_2–Nb_2O_5 phase diagram are discussed in the context of structural chemistry and energy storage properties.